Acta Materialia 240 (2022) 118367

Contents lists available at ScienceDirect

Acta Materialia

journal homepage: www.elsevier.com/locate/actamat

Ni solute segregation and associated plastic deformation mechanisms into random FCC Ag, BCC Nb and HCP Zr polycrystals

Eve-Audrey Picard [a], Frederic Sansoz [a,b,*]

[a] Department of Mechanical Engineering, The University of Vermont, Burlington, VT 05405, USA
[b] Materials Science Program, The University of Vermont, Burlington, VT 05405, USA

ARTICLE INFO

Article history:
Received 17 February 2022
Revised 15 September 2022
Accepted 15 September 2022
Available online 16 September 2022

Keywords:
Grain boundary segregation
Nanocrystalline alloys
Strain localization

ABSTRACT

Different types of grain-boundary (GB) solute segregation in nanocrystalline alloys have been described in the literature as being either homogeneous or heterogeneous, which differently impacts their mechanical properties. In heterogeneous segregation, solute atoms tend to cluster along certain GB areas, while other GB regions remain solute-free. This phenomenon is evidenced with the segregation of Ni solute in nanocrystalline FCC Ag. Yet the physical origin for this segregation behavior and its existence in non-FCC alloys are not fully determined. Here, hybrid Monte-Carlo and molecular dynamics simulations were used to study the segregation of Ni solutes (4 at.%) into nanocrystalline FCC Ag, BCC Nb and HCP Zr metals at their solubility limit temperature and the same homologous temperature ($0.405 \cdot T_m$), respectively. A range of segregation configurations was found: Fully heterogeneous segregation in $Ag_{96}Ni_4$ at 500 K, homogeneous segregation with second-phase precipitates in $Nb_{96}Ni_4$ at 1110 K, homogeneous segregation with dispersion of small-scale Ni clusters in $Nb_{96}Ni_4$ at 1564 K and $Zr_{96}Ni_4$ at 464 K, and fully homogeneous segregation with amorphous intergranular films in $Zr_{96}Ni_4$ at 1118 K. We rationalize these changes by quantifying the Ni solute interactions at GBs. Furthermore, significant variations in mechanical behavior and associated plastic deformation mechanisms are shown for each alloy due to their different segregation behaviors. It is found that strain-localized shear banding is the most significant at interfaces with homogeneous solute segregation containing second-phase precipitates and absent with segregation leading to amorphous intergranular films. These findings underscore the importance of solute interactions in profoundly altering segregation and mechanical behavior in stable nanocrystalline alloys.

1. Introduction

Nanocrystalline (NC) metals with a grain size smaller than 100 nm exhibit superior tensile strength and hardness at ambient temperature compared to their coarse-grained counterparts, but their strengths dramatically decrease at high temperature [1, 2]. Although extreme grain refinement produces a large fraction of GBs impeding the motion of dislocations, exposure to temperature induces GB sliding, GB amorphization and grain growth by GB migration and GB atom diffusion [3–5]. For NC alloys, however, an efficient strategy is to stabilize the structure of the GB network by segregation of solute atoms to the interfaces [6]. As such, NC alloys are made thermally stable either kinematically by solute drag and chemical ordering mechanisms, which have for objective to pin GBs and decrease their mobility, or thermodynamically by reducing the overall GB network energy that normally drives grain growth [7, 8], which is mostly accomplished by substitutional GB solute atoms [9]. Therefore, understanding GB solute segregation mechanisms at atomic scale is critically important for predicting the mechanical properties of NC alloys.

Theoretically, the classical "average" thermodynamical approach by McLean [10] predicts the local solute content at GBs in the dilute limit, i.e. without solute interactions, such as:

$$\bar{X}^{GB} = \left[1 + \frac{1 - X^c}{X^c} \exp\left(\frac{\Delta \bar{E}^{seg}}{kT}\right)\right] \tag{1}$$

where X^c and $\bar{X}^{GB}$ are the average solute contents in the grain interior and the GB network, respectively, $\Delta \bar{E}^{seg}$ is the average solute segregation energy in the GB network, T is the temperature, and k is the Boltzmann constant. A difference in atomic size between solute and solvent [6], low solubility and low diffusivity [7] are a few factors enhancing the GB segregation energy. In recent years, however, a more detailed picture has emerged where GB segregation

* Corresponding author.
E-mail address: frederic.sansoz@uvm.edu (F. Sansoz).

https://doi.org/10.1016/j.actamat.2022.118367

energy in polycrystals is classified by the availability of atomic GB sites associated with different local environments that either promote or impede segregation at atomic scale [11–13]. Wagih and Schuh [14–16] have proposed an efficient approach based on the spectral analysis of local GB segregation energy in polycrystals by adapting the McLean equation to atomistic models, while Matson and Schuh [17] have recently extended the same spectral analysis to GB solute interaction energy. These studies show that both the spatial distribution of high and low GB segregation energy sites and intrinsic GB solute interactions have become critically important for understanding solute segregation behavior in NC alloys. In fact, these authors proposed that the segregation behavior is largely dominated by the negative (most favorable) tail of the segregation energy spectra.

Experimentally, the complex nature of GB solute interaction is often manifested in NC alloys by the formation of heterogeneous solute atom clusters or precipitates along GB interfaces and triple junctions, as well as, by GB anisotropy with significant variations of solute content between different GBs [18–23]. Heckman et al. [24] have revealed that heterogeneous Au segregation results in higher resistance to cracking and increased fracture toughness in immiscible NC Pt-Au alloys, compared to alloys with homogeneous segregation. Furthermore, Pan et al. [25] proposed a theory to quantify GB solute interactions by calculating the solute dipole formation energy obtained from the difference of potential energy between a GB with two solute atoms in a split configuration to another configuration containing a dipole of bonded solute atoms. In the case of Ni segregation into Ag bicrystals, density-functional-theory (DFT)-based calculations have suggested that the Ni dipole formation energy at GB is as high as 0.0771 eV corresponding to a strong tendency for Ni clustering at crystalline interfaces. Concurrently, Pan and Sansoz [26] have predicted by atomistic simulation that Ni solute segregation behavior in a 6-nm-grain-diameter Ag polycrystal is fully heterogeneous, with significant Ni-rich clusters forming at random GBs and GB triple junctions, which is consistent with the hypothesis of the bicrystal study in [25]. Also, an experimental study by Santhi et al. [27] has observed the precipitation of Ni solute atoms at GBs in consolidated NC $Ag_{75}Ni_{25}$ alloys annealed at 500 °C.

Most alloys where heterogeneous GB solute segregation has been observed in the literature are face-centered cubic (FCC), e.g. Ag-Ni, Pt-Au [21], and Ni-P [28], whereas GB segregation in other NC FCC alloys such as Cu-Zr [29], Al-Ni-Y [30, 31], and Al-Ni-Ce [32] has proven to be fully homogeneous with the formation of amorphous interfacial films. There is only one recent example of heterogeneous segregation in a non-FCC alloy, Cr-segregation into a body-centered cubic (BCC) Fe polycrystal [33]. Since Ni solute segregation gives rise to clustering at FCC Ag GBs, an important question is whether the Ni solute clustering at GBs leading to heterogeneous segregation behavior is more generally present in binary alloys with different crystal structures, e.g., BCC and hexagonal-closed packed (HCP) structures. This work presents the first atomistic study providing a direct comparison between systems with these different crystal structures.

In this article, hybrid Monte Carlo/Molecular Dynamics (MC/MD) simulations are used to study the effects of crystal structure (FCC, BCC and HCP) on segregation behavior in random polycrystals containing the same concentration of Ni solute (4 at%), and their tensile plastic deformation mechanisms at room temperature. The studied binary alloys are $Ag_{96}Ni_4$ (FCC), which is acting as our reference system, $Nb_{96}Ni_4$ (BCC) and $Zr_{96}Ni_4$ (HCP) at their maximum solubility temperature and the same homologous temperature of $0.405{\cdot}T_m$, respectively, where T_m is the melting temperature of the studied alloy. This article is divided as follows. Section 2 covers the computational methodology. The results and structural analysis of simulated segregation in each alloy are presented in Section 3. Section 4 focuses on the simulation of plastic deformation mechanisms during tensile deformation of each segregated alloy, in comparison to the mechanical behavior of pure FCC Ag, BCC Nb and HCP Zr polycrystals. Section 5 discusses the role played by GB solute interactions on GB solute clustering mechanisms in NC alloys and the physical origin for strain localization mechanisms in random polycrystals with GB solute clustering or GB precipitation.

2. Methodology

2.1. Hybrid MC/MD simulation

All MC/MD simulations were performed with the software LAMMPS [34] on the supercomputer Cori at the National Energy Research Scientific Computing Center (NERSC). A generalized form of the embedded-atom-method potential based on Finnis-Sinclair formalism was used to compute each pair interaction in Ag-Ni [25], Nb-Ni [35], and Zr-Ni [36] binary alloys. The simulations were performed in a variance-constrained semi-grand-canonical (VC-SGC) ensemble following the same methodology as described in [26]. MC trials were run with constant parameters c_0, $\Delta\mu_0$, and κ which are, respectively, the total solute concentration, the chemical potential difference between the elements of the system acting as an effective average constraint, and the variance constraint parameter. We used $\kappa = 2000$, which led to fewer oscillations about c_0, noting that the average concentration did not change significantly with higher κ values. The concentration c_0 was fixed at 4 at.% Ni for all simulations, because previous MC/MD simulations by Pan and Sansoz [26] predicted that this concentration caused strengthening with the occurrence of shear localization in NC Ag-Ni polycrystals with a mean grain size of 6 nm. The chemical potential difference $\Delta\mu_0$ was varied for each simulated alloy as shown in Table 1. To obtain these values, κ was first temporarily set to 200, which allowed for more significant variation of $\Delta\mu_0$ at each time step until $\Delta\mu_0$ was stabilized within ± 0.05 eV between timesteps. The MC/MD was then restarted from the stabilized $\Delta\mu_0$ value with $\kappa = 2000$. This procedure was conducted at each temperature for all alloys.

To ensure proper structural relaxation and chemical mixing, the MC algorithm was interrupted by short MD runs [37]. Each MC cycle consisted of a total number of trial moves equal to the number of atoms in the system and was separated by 1000 MD steps at the same temperature, which was iterated 600 times. MD was performed in the isothermal-isobaric (NPT) ensemble using a Nose-Hoover temperature thermostat and a zero pressure barostat. The MD timestep was 0.001 ps resulting in a total duration of 600 ps. From visual inspection, Ni positions were found nearly identical from one step to the next after that duration.

2.2. Segregation temperatures

The reference $Ag_{96}Ni_4$ alloy is known to exhibit heterogeneous Ni segregation in GBs at a temperature (T) of 500 K [26]. Using the melting point (T_m) of 1235 K for pure Ag [38], the homologous temperature corresponds to $0.405{\cdot}T_m$ for this alloy. First, a series of simulations was conducted with each alloy at a constant homologous temperature of $0.405{\cdot}T_m$ as shown in Table 1. It should be noted that Zr has two different types of crystal structures, HCP α and BCC β phases, respectively. The transition temperature from HCP to BCC ($T_{\alpha\beta}$) is 1147 K [39]. Since an HCP crystal structure was considered for the $Zr_{96}Ni_4$ alloy, we substituted T_m by $T_{\alpha\beta}$ to ensure that all temperatures were in the α-phase. Second, a series of MC/MD simulations was carried out in the BCC $Nb_{96}Ni_4$ alloy and HCP $Zr_{96}Ni_4$ alloy at their maximum solubility temperature to reduce the formation of second-phase precipitates. This step was not

Table 1
MC/MD simulation parameters for each studied alloy and temperature. *For Zr-Ni, $T_m = T_{\alpha\beta}$, where $T_{\alpha\beta}$ is the transition temperature between the HCP and BCC phase for Zr. The cutoff radius (R_{cutoff}) value in parenthesis corresponds to that used for the pure metal.

Alloy	FCC $Ag_{96}Ni_4$	BCC $Nb_{96}Ni_4$		HCP $Zr_{96}Ni_4$	
Temperature T (K)	500	1110	1564	464	1118
$\Delta\mu_0$ (eV)	1.015	−2.499	−2.420	−1.440	−1.080
T_m (K)	1235	2742	2742	1147*	1147*
T / T_m	0.405	0.405	0.570	0.405	0.975
R_{cutoff} (Å)	3.585 (3.585)	3.945 (3.975)	4.005	3.885 (3.855)	3.915

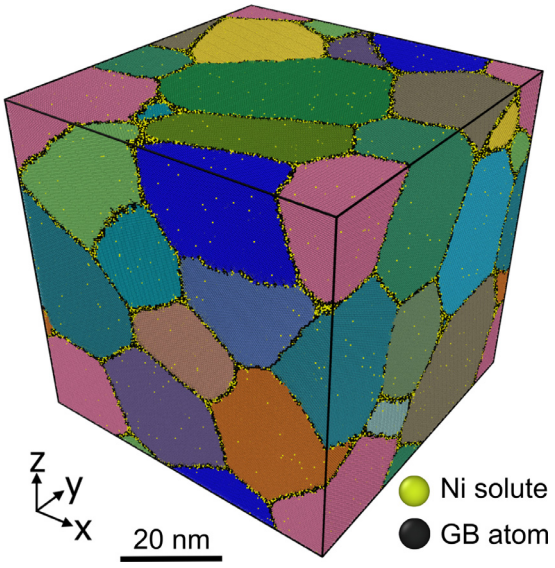

Fig. 1. Atomistic snapshot of a BCC Nb polycrystal with a solute content of 4 at.% Ni after MC/MD simulation at 1564 K represented using the polyhedral template matching and grain segmentation analysis. Grains are colored according to their crystallographic orientation.

required for FCC $Ag_{96}Ni_4$, because this alloy is immiscible. For Nb-Ni, the maximum solubility occurs at the eutectoid temperature of 1564 K [38]. For Zr-Ni, to ensure that the crystal remains HCP, the maximum solubility temperature was chosen at 1118 K, which is 2.5% lower than the temperature transition $T_{\alpha\beta}$.

2.3. Polycrystal models

Three atomic models of random FCC, BCC and HCP polycrystals were created using the program Atomsk [40]. The total number of atoms per model was ~12 million. The simulation box for each polycrystal had an equal length of 60 nm in the x, y, and z directions. All boundaries were periodic. The total number of grains was kept constant at 27 corresponding to an average grain size of ~24 nm. All polycrystals had grains originating at the same positions and were oriented in the same directions to maintain similar configurations. The lattice constant a for FCC Ag was 4.16 Å [25] and 3.3004 Å for BCC Nb [41]. The a and c lattice parameters for HCP Zr were 3.232 Å and 5.147 Å, respectively [42]. Fig. 1 represents an atomistic snapshot of a BCC Nb polycrystal after MC/MD simulation at the maximum solubility temperature of 1564 K using the polyhedral template matching and grain segmentation analysis in the software OVITO [43]. In this example, we found no increase in average grain size at high temperature, i.e., the grain size before and after MC/MD at 1564 K was 24.3 ± 3.6 nm and 23.6 ± 5.7 nm, respectively, which is attributed to the stabilizing effect of the Ni solute at GBs. In fact, a slight reduction of grain size was noticeable after solute segregation due to GB atom relaxation and amorphization.

Furthermore, Wagih and Schuh [15] have proven that the GB misorientation angle distribution is random in polycrystals made by the same method. By inspecting our models in the software OVITO, we found that our polycrystals contained mostly high-angle general GBs, with only one or two low-angle GBs. Therefore, the GB structure of the simulated polycrystals was also considered to be random in the present study.

2.4. Solute cluster analysis

The radial distribution function (RDF) for Ni-Ni pairs was used to analyze the structure of Ni atom clusters among GB atoms. In theory, the shape of the RDF gives insight into the predominant interatomic distances between atoms in a cluster, resulting in different peaks [44]. The peaks of the RDF curves for each alloy representing the distances between the atoms of Ni at GBs was compared to the peaks produced by the RDF of a perfect FCC Ni unit cell. The first and second peaks are, respectively, the nearest and second nearest neighbor (NN) distances. The first, second, third, and fourth NN distances are $a\sqrt{2}/2$, $a\sqrt{3}/2$, a, and $a\sqrt{2}$, respectively. The NN distances were obtained from the Ni FCC atom arrangement with a lattice constant a of 3.52 Å [45]. Therefore, the NN distances for Ni in order from the first to fourth NN were 2.49 Å, 3.05 Å, 3.52 Å, and 4.98 Å, respectively. Additional peaks were attributed to the presence of other arrangements of Ni atoms such as precipitates within the structure.

2.5. Local solute density

To quantify the heterogeneity in solute concentration at GBs, we calculated the local Ni density within a spherical volume surrounding each GB atom site. The GB atoms were identified by the common neighbor analysis (CNA) implemented in OVITO using the cutoff radii given in Table 1. The cutoff radius was chosen as the minimum distance of the second RDF peak for the specific alloy to ensure full inclusion of the first NN. The local density was calculated by iterating through all GB atoms including the solvent atoms. For each iteration, the current atom represented the center atom of a local sphere of radius set to 1 nm, which corresponds approximately to the average GB thickness in GB-segregated alloy polycrystals [46]. The local density was obtained by dividing the total number of Ni atoms within the local sphere centered on each GB atom by the spherical volume.

2.6. Tensile deformation and shear localization

Before deformation, each model was cooled down to 300 K at 2 K/ps under zero pressure using NPT integration and a timestep of 0.002 ps. The models were then maintained at 300 K for another 100 ps. Tensile deformation was simulated by stretching the simulation box along the x-axis at a constant engineering strain rate of $10^8\ s^{-1}$ up to 10% strain, while zero pressure was imposed in the y and z directions using NPT integration. No significant change in behavior was observed at a lower strain rate (Supplementary Figure). The timestep was 0.005 ps during deformation. The total strain was calculated by multiplying the engineering

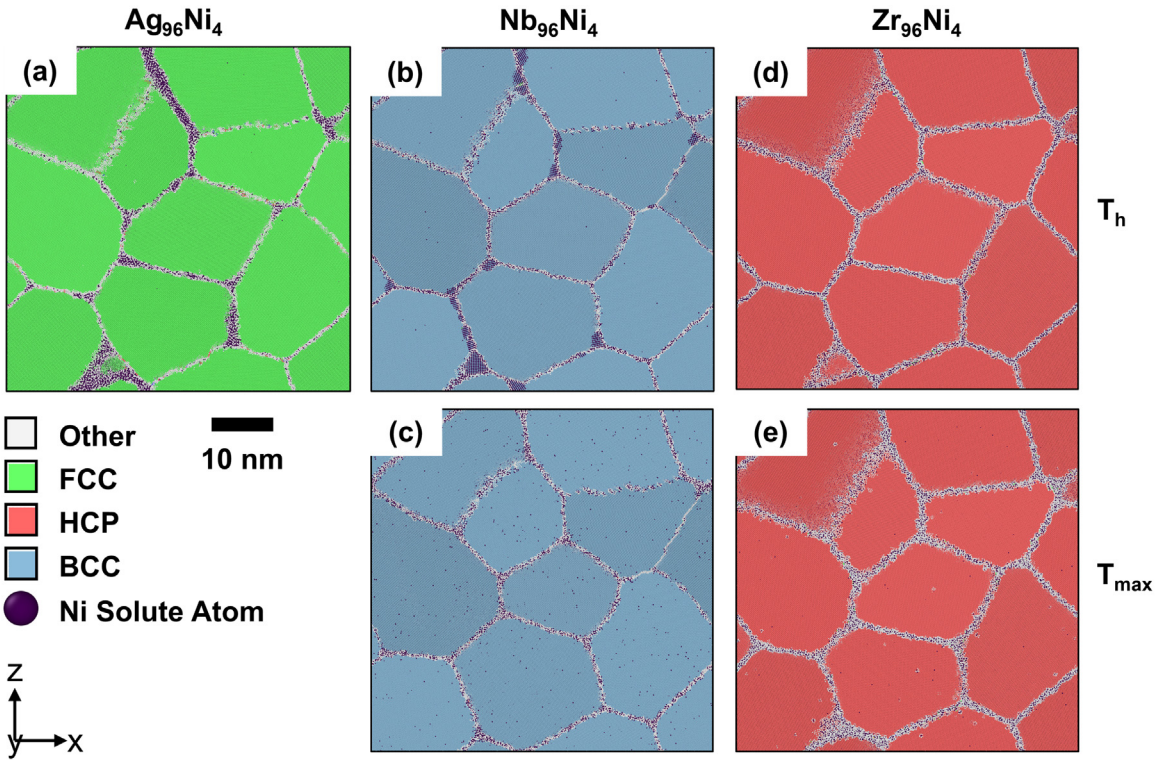

Fig. 2. Equilibrium segregation of Ni solute atoms in random polycrystals in (a) $Ag_{96}Ni_4$ at 500 K, (b) $Nb_{96}Ni_4$ at 1110 K, (c) $Nb_{96}Ni_4$ at 1564 K, (d) $Zr_{96}Ni_4$ at 464 K, and (e) $Zr_{96}Ni_4$ at 1118 K. Here $T_h = 0.405 \cdot T_m$ and T_{max} is the maximum solubility temperature for each specific alloy.

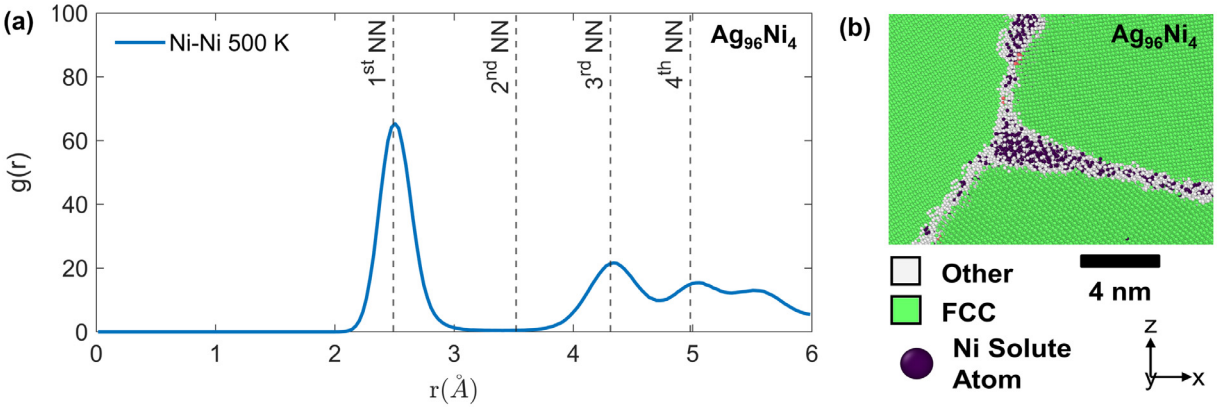

Fig. 3. Grain-boundary structural analysis in a segregated $Ag_{96}Ni_4$ polycrystal. (a) RDF curve for Ni –Ni pairs at GBs and (b) Ni solute distribution at a representative GB triple junction in $Ag_{96}Ni_4$ at a homologous temperature of $0.405 \cdot T_m$. The first four nearest-neighbor (NN) distances in a perfect FCC Ni unit cell are indicated by dashed lines.

strain rate with the time elapsed in the simulation. The stress was calculated from the box pressure retrieved along the x-axis. Simulation snapshots were extracted at 5 ps intervals. The atomic von Mises shear strain was obtained from the Green-Lagrangian strain tensor in OVITO. The range of neighbors considered for the strain calculation was based on the cutoff radii in Table 1.

3. Segregation results

3.1. Segregation differences

Fig. 2 shows that the segregation behavior of Ni solute (4 at.%) is markedly different between FCC Ag, BCC Nb, and HCP Zr polycrystals. In Fig. 2(a), segregation in the $Ag_{96}Ni_4$ polycrystal at 500 K is fully heterogeneous. It is characterized by large Ni clusters in some areas of the GB network, while other GB regions have fewer or no Ni atoms, which agrees well with previous MC/MD results in Ag-Ni alloys with different solute content and grain size [26].

In Fig. 2(b), ordered Ni-rich precipitates are detected within the $Nb_{96}Ni_4$ polycrystal at the same homologous temperature (i.e., $T_h = 0.405 \cdot T_m = 1110$ K). In this case, the precipitates are concentrated at GB triple junctions, whereas GB interfaces without noticeable precipitation show a more uniform dispersion of Ni solute atoms. Therefore, we define this type of segregation in $Nb_{96}Ni_4$ as being a homogeneous GB segregation with second-phase precipitation. In Fig. 2(c), we observed that more Ni atoms tend to be attracted towards GB triple junctions in the $Nb_{96}Ni_4$ polycrystal at its maximum solubility temperature (i.e., $T_{max} = 1564$ K). Contrary to the polycrystal at T_h, however, no distinct precipitates are present at the junctions at T_{max}. Also, in Fig. 2(c), a homogeneous distribution of small Ni clusters is seen all around GBs, which is absent

at T_h in Fig. 2(b). These differences manifested between low and high temperatures suggest that the Ni-rich precipitates at homologous temperature are redissolved into nanoscale Ni clusters at the solubility limit temperature in $Nb_{96}Ni_4$ polycrystals.

Furthermore, in Fig. 2(d) and 2(e), both $Zr_{96}Ni_4$ polycrystals do not show any sign of precipitation or clustering, suggesting a fully homogeneous Ni solute segregation to GBs. However, in Fig. 2(e), the segregated GB region is noticeably thicker at the solubility limit temperature T_{max} = 1118 K than at the equivalent homologous temperature T_h = 464 K, which has been observed in past experimental studies on some nanocrystalline alloys with intergranular amorphous films such as NC Cu-Zr [29], NC Al-Ni-Y [30, 31], and NC Al-Ni-Ce [32]. In fact, sputter-deposited thin films of Zr-4 at.%Ni have also been found to form ultra-fine grains with a significant fraction of amorphous phase at GBs [47].

3.2. GB structural analysis

The RDF curve obtained for the GB network in the $Ag_{96}Ni_4$ alloy is presented in Fig. 3(a). For comparison, we superimposed the first four NN distances of a crystal with perfect FCC Ni unit cell. Fig. 3(a) shows good agreement between the first peak from the left of this RDF and the 1st NN distance in a perfect FCC Ni unit cell, which indicates that the first peak coincides with the ability of solute atoms to form Ni dipoles with one another in the GBs [48]. Also, the first peak is high, suggesting that Ni-Ni solute interaction is strongly favored inside GBs of the Ag matrix and that $Ag_{96}Ni_4$ is prone to Ni atom agglomeration and cluster formation at GBs.

However, Fig. 3(a) shows that the second peak of this alloy RDF does not match with the 2nd NN distance of the FCC Ni unit cell. This result signifies that Ni solute atoms have an amorphous arrangement. In the microstructure, this conclusion is confirmed by the formation of large amorphous Ni clusters at GB triple junctions, as shown in the example in Fig. 3(b). Because GB atoms in random polycrystals are considered to have an amorphous arrangement, the position of the second RDF peak in amorphous materials is generally shifted further to the right to a wider range of large distances [49], compared to more crystalline materials. The RDF curve in Fig. 3(a), however, is split into multiple secondary sub-peaks to the right, which are close to the 3rd NN and 4th NN distances of the FCC Ni crystal. This phenomenon is similar to the RDF of FCC Au nanoclusters, where multiple secondary peaks occur when the cluster size increases [44]. In fact, Ding et al. [50] have noted that a split of the second peak of the RDF curve of amorphous metals and alloys was related to the formation of 2-atom, 3-atom and 4-atom ordered cluster connections inside the amorphous phase. Therefore, the presence of multiple secondary peaks aligned with the 3rd NN and 4th NN distances of the FCC crystal could be attributed to small and ordered Ni solute clusters inside the GBs of the $Ag_{96}Ni_4$ polycrystal.

Furthermore, Fig. 4(a) presents the RDF curves for the $Nb_{96}Ni_4$ polycrystal at both homologous and solubility limit temperatures. At T_h = 1110 K, the RDF curve features a split of the first peak unlike all other models in this study. In effect, precipitates are present at GB triple junctions, as seen at temperature T_h in Fig. 4(b), and are totally absent at higher temperature T_{max} in Fig. 4(c) when the RDF split disappears in Fig 4(a).

To gain insight into the occurrence of a split, we computed the RDF curve for Ni atom distances in a specifically large precipitate formed in the polycrystal as shown in Fig. 5(a). Fig. 5(b) reveals that the precipitate has the composition of an Nb_7Ni_6 stoichiometric compound [38]. The peaks of the RDF curve extracted from the precipitate and labelled as A, B, and C in Fig. 5(c) were superimposed to the RDF curve of the whole $Nb_{96}Ni_4$ polycrystal shown in inset. The precipitate peak positions are found to match with the positions of the split of the first peak, the second peak and third peak of the $Nb_{96}Ni_4$ polycrystal RDF in Fig. 4(a), whereas the 2nd, 3rd, and 4th NN distances in the perfect FCC Ni unit cell are different. This result provides evidence that the presence of anomalous peaks in the RDF of $Nb_{96}Ni_4$ alloy at 1100 K is due to the formation of highly ordered precipitates and is not an indication of solute segregation behavior or clustering in this specific alloy. This conclusion implies that GB areas without precipitation have probably limited Ni crystallization at all temperatures. Furthermore, although the first RDF peaks of the $Nb_{96}Ni_4$ polycrystal are smaller than that of the $Ag_{96}Ni_4$ polycrystal, this alloy can be considered prone to small-scale Ni solute clustering at both temperatures. Therefore, GB segregation behavior in $Nb_{96}Ni_4$ polycrystals qualifies as a homogeneous segregation with dispersion of small-scale Ni clusters at all temperatures, and the additional presence of Nb_7Ni_6 precipitates at lower temperature T_h.

Moreover, Fig. 6(a) shows that the position of the first peak in the $Zr_{96}Ni_4$ polycrystal coincides with the 1st NN distance of Ni interactions. The second peak of $Zr_{96}Ni_4$ at T_h = 464 K follows the RDF profile previously discussed in the literature for glasses and liquids [50] and is characterized by a split commonly observed with amorphous metals and, thus confirms that the Ni solute distribution in the GB network is amorphous. Also, from the shape of the second peak at 464 K, it is possible to infer the presence of few-atom Ni clusters in the GBs. Therefore, GB segregation in the $Zr_{96}Ni_4$ polycrystal at 464 K is considered similarly to that in the $Nb_{96}Ni_4$ polycrystal at 1564 K, i.e., a homogeneous dispersion of small-scale Ni nanoclusters.

The RDF curve in $Zr_{96}Ni_4$ at T_{max} = 1118 K presents less distinction in the peaks, while the formation of Ni dipoles is also less evident than at 464 K based on the size of the first peak. This smoother curve is a representation of a less ordered, but more uniform Ni distribution with a significant decrease in clustering. This result is accompanied by thickening of the amorphous GB region when the temperature increases from T_h to T_{max}, as manifested in Fig. 6(b) and Fig. 6(c), respectively.

To support the indirect RDF results, Fig. 7 represents a close-up view of the different Ni clustering behavior at a same GB triple junction in each alloy. This figure confirms qualitatively that Ni solute clustering decreases from larger Ni clusters in FCC $Ag_{96}Ni_4$ to smaller few-atom Ni clusters in BCC $Nb_{96}Ni_4$ at 1564 K and HCP $Zr_{96}Ni_4$ at 464 K, and no significant clustering in HCP $Zr_{96}Ni_4$ at 1118 K.

3.3. Local solute density

Profiles of the local solute density distribution inside the random GBs are presented in Fig. 8 to quantify the significance of Ni solute clustering in the GB network across the different models. The local density distribution in the reference $Ag_{96}Ni_4$ polycrystal in Fig. 8(a) is noticeably different from that of the other binary alloys, due to fully heterogeneous Ni segregation at GBs. This density spectrum characteristically exhibits two major peaks. The first peak corresponds to solute-starved GB areas containing less than 5 Ni atoms/nm^3. The second peak spans a wide range of larger solute densities from 10 to 40 Ni atoms/nm^3 in other GB regions with distributions of amorphous Ni clusters that can be small or large, as shown in Fig. 2(a).

In contrast, in Figs. 8(b)-(c), local Ni density profiles in the $Nb_{96}Ni_4$ polycrystal present a single peak with a similar skew-normal distribution at all temperatures. The density peaks are slightly skewed to the right with local solute densities attaining high values from 15 to 30 Ni atoms/nm^3. At 1110 K, this effect could be attributed to the ordered Nb_7Ni_6 precipitates, which are naturally richer in Ni atoms than the rest of the amorphous GBs. Despite the skewness of the curve in Fig. 8(c), however, precipi-

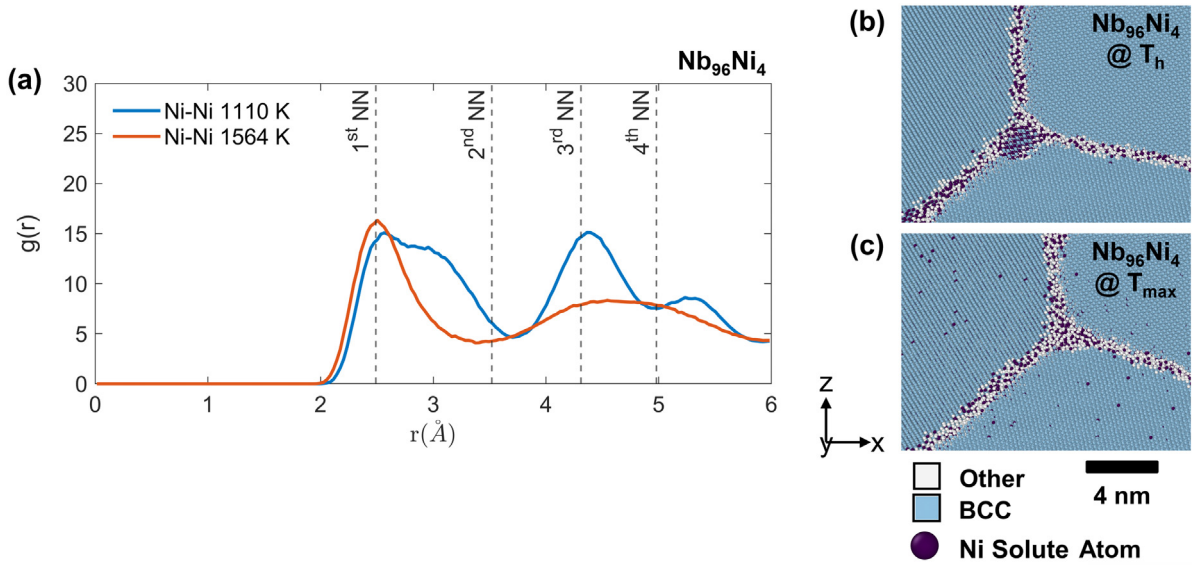

Fig. 4. Grain-boundary structural analysis in segregated $Nb_{96}Ni_4$ polycrystals. (a) RDF curves for Ni-Ni interactions at GBs. Examples of GB triple junction in $Nb_{96}Ni_4$ at (b) $0.405 \cdot T_m$ and at (c) solubility limit temperature T_{max}. The first four NN distances in a perfect FCC Ni unit cell are indicated by dashed lines.

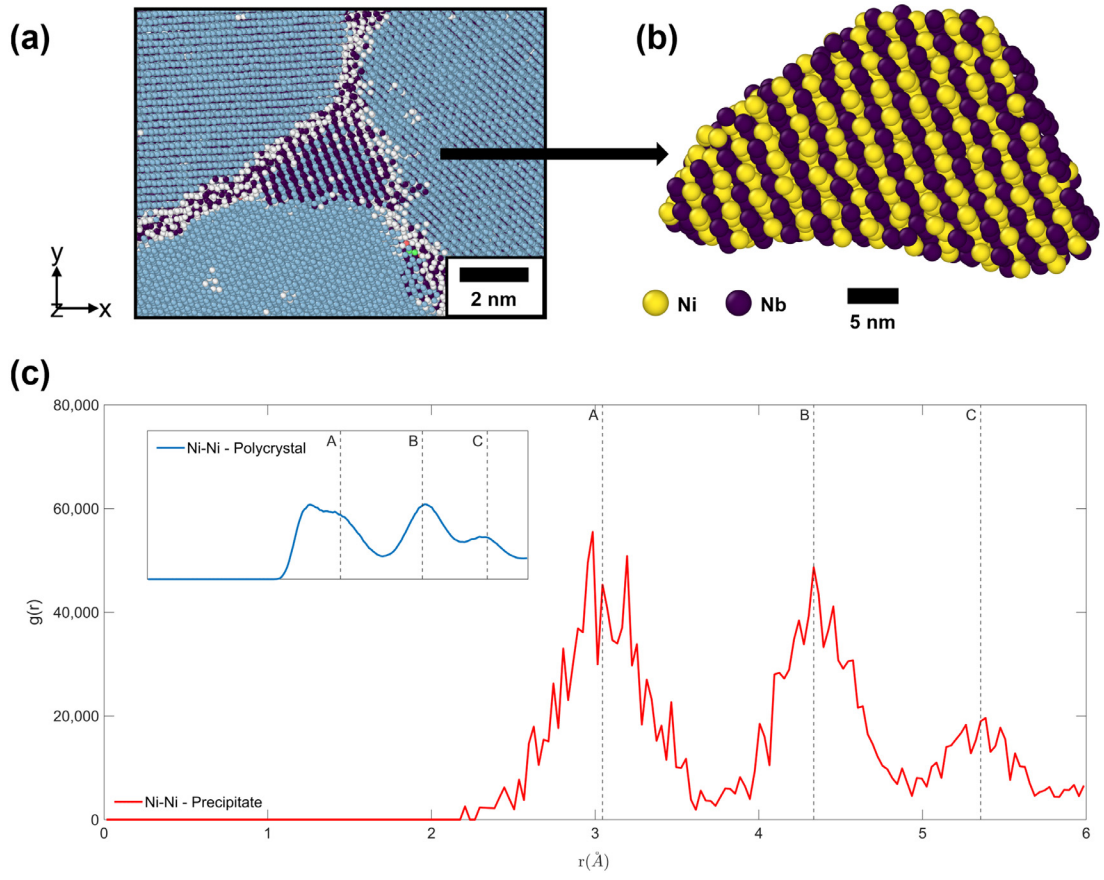

Fig. 5. Structural analysis of precipitates in $Nb_{96}Ni_4$ polycrystal simulated at homologous temperature of 1110 K or $0.405 \cdot T_m$. (a) Close-up view on a GB triple junction with a large Ni-rich precipitate. (b) Chemical composition of the same precipitate. (c) RDF curve of the precipitate for the Ni atoms interaction compared to the RDF for all the Ni atoms in the $Nb_{96}Ni_4$ polycrystal in inset.

tates are absent at 1564 K. A possible reason for the skewed peak is that GB triple junctions where ordered precipitates would be expected to occur at lower temperature exhibit high Ni concentrations from local clustering at 1564 K. This result suggests that the section of the curve with higher local Ni densities in the $Nb_{96}Ni_4$ polycrystals relates to an agglomeration of Ni-rich precipitates or clusters towards GB triple junctions in this alloy. Also, in Figs. 8(b)-(c), the occurrence of a well-defined peak at ~8 Ni atoms/nm^3 indicates that the other GB regions are comprised of a homogeneous distribution of Ni solutes.

Furthermore, local Ni density profiles in the $Zr_{96}Ni4$ polycrystals at 464 K and 1118 K in Fig. 8(d)-(e), respectively, present a

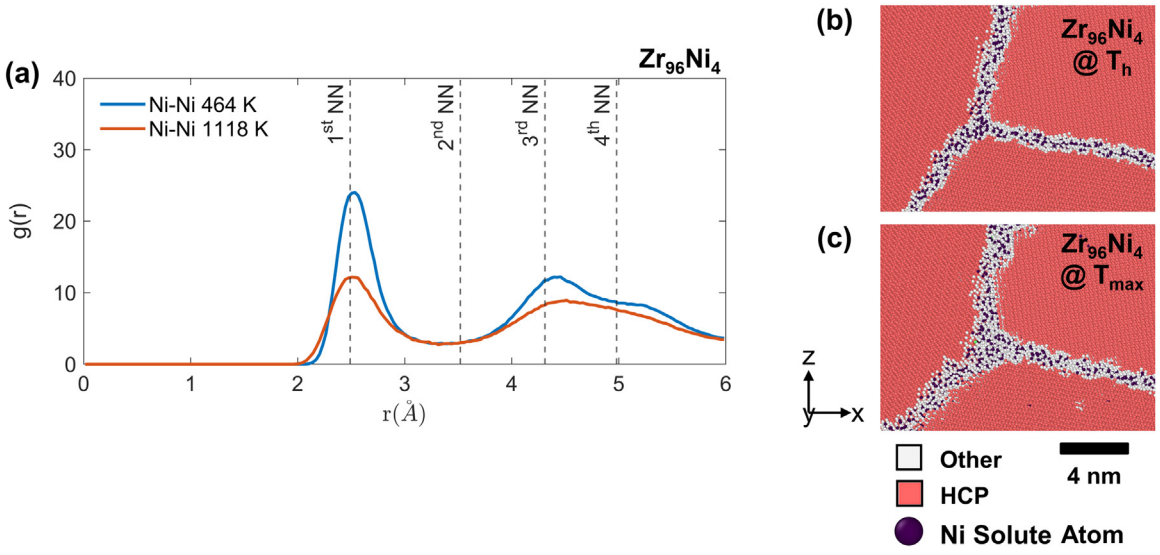

Fig. 6. Grain-boundary structural analysis in segregated $Zr_{96}Ni_4$ polycrystals. (a) RDF curves for Ni-Ni interactions at GBs. Examples of GB triple junction in $Zr_{96}Ni_4$ at (b) $0.405 \cdot T_m$ and at (c) solubility limit temperature T_{max}. The first four NN distances in a perfect FCC Ni unit cell are indicated by dashed lines.

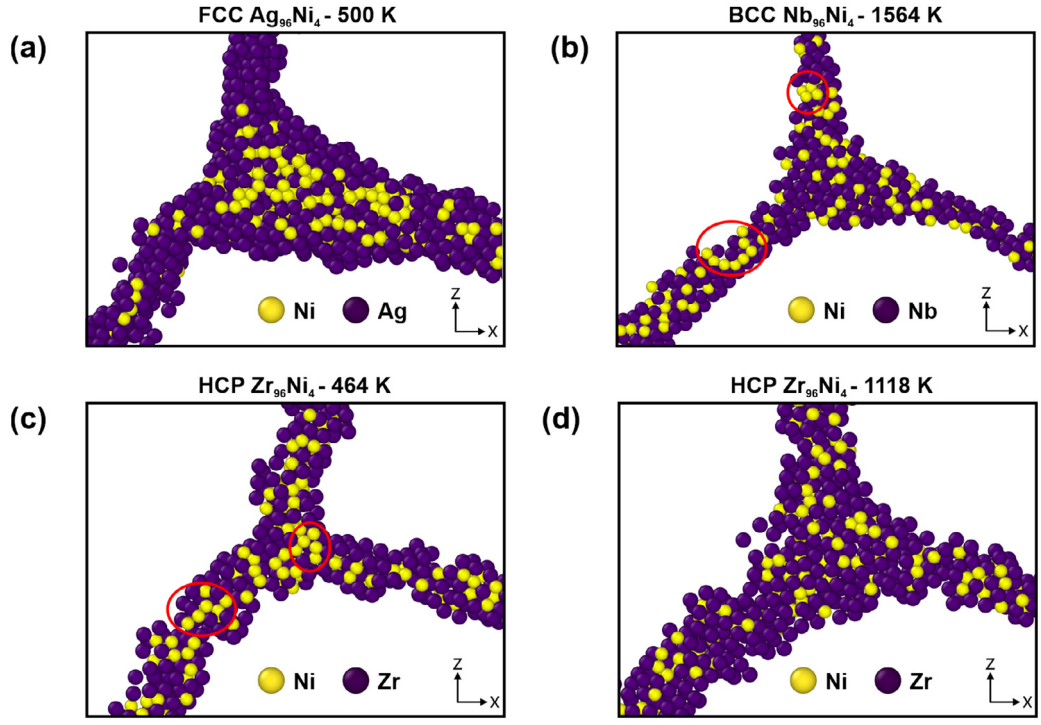

Fig. 7. Local Ni solute clustering at a GB triple junction. (a) A large Ni cluster in $Ag_{96}Ni_4$. Few-atom Ni clusters (circled in red) in (b) $Nb_{96}Ni_4$ at 1564 K and (c) $Zr_{96}Ni_4$ at 464 K. (d) No significant clustering evidenced in $Zr_{96}Ni_4$ at 1118 K. Only GB atoms are shown for clarity.

more defined single peak with a statistically normal distribution centered at 8 Ni atoms/nm^3, which confirms that the segregation behavior is more homogeneous in this alloy than in the others. Also, it is worth noting that the RDF analysis in Fig. 6 led to the conclusion that GBs in $Zr_{96}Ni_4$ displayed more Ni atom ordering at 464 K than at 1118 K, which did not result in marked differences in local density profiles in Fig. 8(d)-(e). This result proves that Ni atom ordering at GBs must remain relatively small and localized in the $Zr_{96}Ni_4$ alloy.

4. Plastic deformation mechanisms

4.1. FCC Ag polycrystals

Tensile stress-strain curves for pure Ag and $Ag_{96}Ni_4$ polycrystals deformed at 300 K are represented in Fig. 9, along with three snapshots of the distribution of atomic von-Mises shear strain at 2, 6, and 10% applied strains. The curve shape in the reference $Ag_{96}Ni_4$ polycrystal after GB segregation presents three major dif-

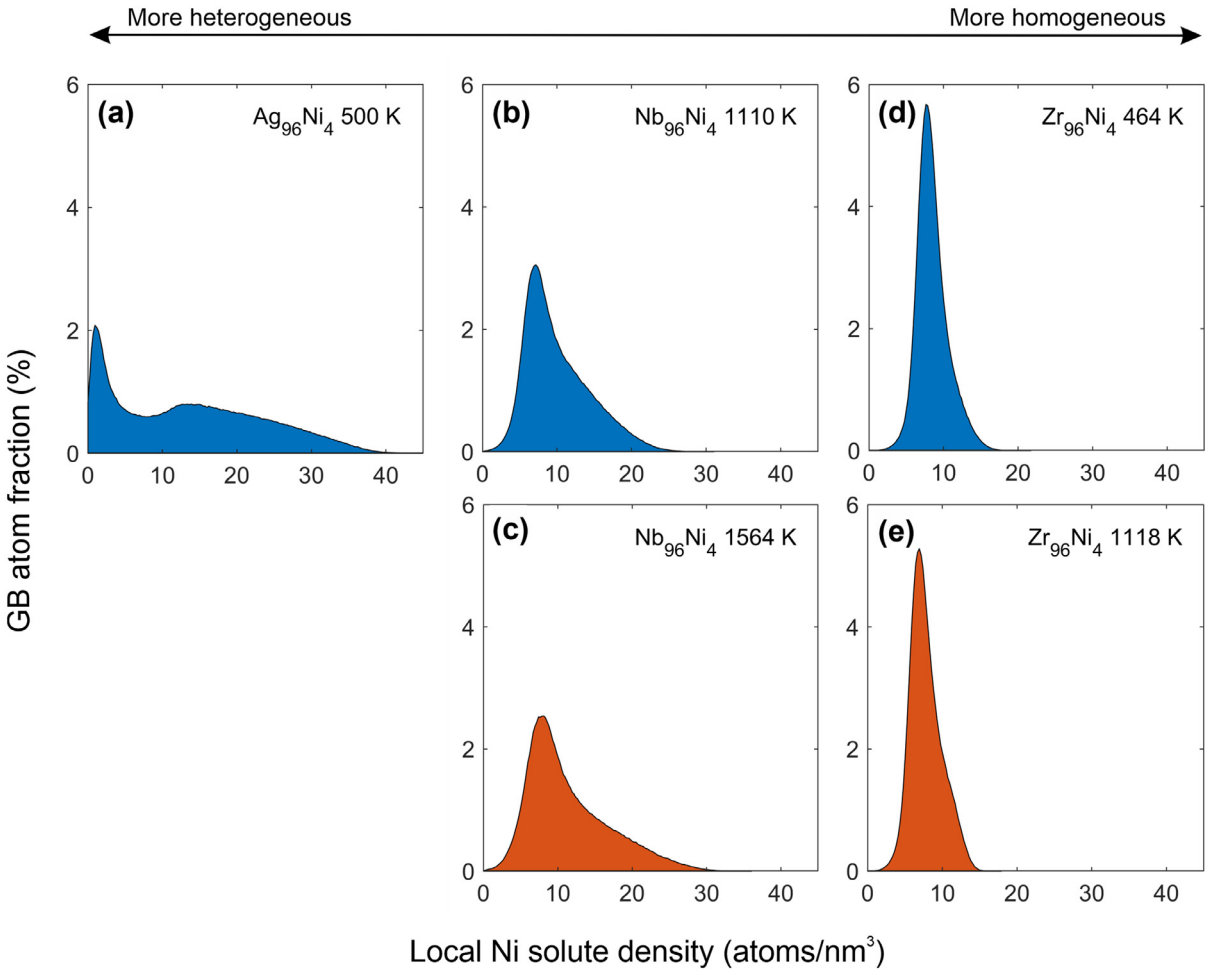

Fig. 8. Profiles of local Ni solute density distribution in network of random GBs in (a) $Ag_{96}Ni_4$ at 500 K, (b) $Nb_{96}Ni_4$ at 1110 K, (c) $Nb_{96}Ni_4$ at 1564 K, (d) $Zr_{96}Ni_4$ at 464 K, and (e) $Zr_{96}Ni_4$ at 1118 K.

ferences compared to that in pure Ag metal. First, GB segregation increases the initial strain at yield point as shown in snapshot 1 where deformation is uniform with no significant GB plasticity or amorphization at 2% applied strain. Subsequently, the stress-strain curve in $Ag_{96}Ni_4$ exhibits a stress peak of 1.78 GPa at 3.2% strain, a 40% increase from that in pure Ag, followed by an abrupt stress drop due to GB-mediated dislocation nucleation and GB plasticity as shown in snapshot 2.

Third, a plateauing at an average flow stress of 1.3 GPa is evidenced from 6% to 10% applied strains. Apparently, at 10% applied strain, snapshot 3 shows some signs of shear band formation by strain localization across multiple grains. This type of mechanical behavior has been reported in the literature in other nanocrystalline or amorphous metals exhibiting similar shear localization mechanisms. For example, Pan and Sansoz [26] have studied the plasticity of different Ag-Ni polycrystals with a grain size averaging 6 nm and noted that shear localization was persistent with Ni content up to 8 at.% and was suppressed for larger Ni contents. They proposed that, at low solute content, Ni clusters at GB triple junctions were too small to effectively impede shear banding across grains, which is most likely the case in the current polycrystal model that has a larger grain size. Furthermore, Steif et al. [51] have previously described that the stress-strain response due to shear-band softening in amorphous metals is typically characterized by a pronounced stress peak followed by stress plateauing from uniform shearing, because free volume expansion in the shear strain-localized zone induces a catastrophic softening. However, the shear bands in amorphous metals do not grow once the stress is leveling [52]. Likewise, Feng et al. [53] have predicted by MD simulation that $Zr_{70}Cu_{30}$ metallic glasses reach a peak at yielding point, followed by strain-softening to a steady-state stress plateau, coinciding with the growth of porosity.

4.2. BCC Nb polycrystals

The stress-strain curves for pure Nb and $Nb_{96}Ni_4$ polycrystals segregated at 1110 K and 1564 K are compared in Fig. 10. The curve in $Nb_{96}Ni_4$ at 1110 K reaches a maximum stress of 6 GPa at 5% applied strain, before plateauing between 8% and 10% applied strain. Snapshots of the distribution of atomic von-Mises shear strain show that a major shear band forms and propagates through several GBs and grains when the maximum stress is reached. The shear band becomes increasingly thicker up to 10% strain as seen in snapshot 3 in the $Nb_{96}Ni_4$ polycrystal segregated at 1110 K. We attribute this behavior to the position of precipitates at GB triple junctions extending from the grain interior to the GBs. The sites formed by the interface of the main matrix and a precipitate are known to initiate and help propagate cracks, which is ultimately induced by shear localization at GBs [54]. Furthermore, as shown above in Section 3, the $Nb_{96}Ni_4$ polycrystal at 1564 K did not contain precipitates, but it was found to produce a dispersion of small Ni solute clusters within GBs. Snapshots in Fig. 10 show that Ni clusters in $Nb_{96}Ni_4$ at 1564 K have limited the growth of shear bands and inhibited shear localization mechanisms. Therefore, the

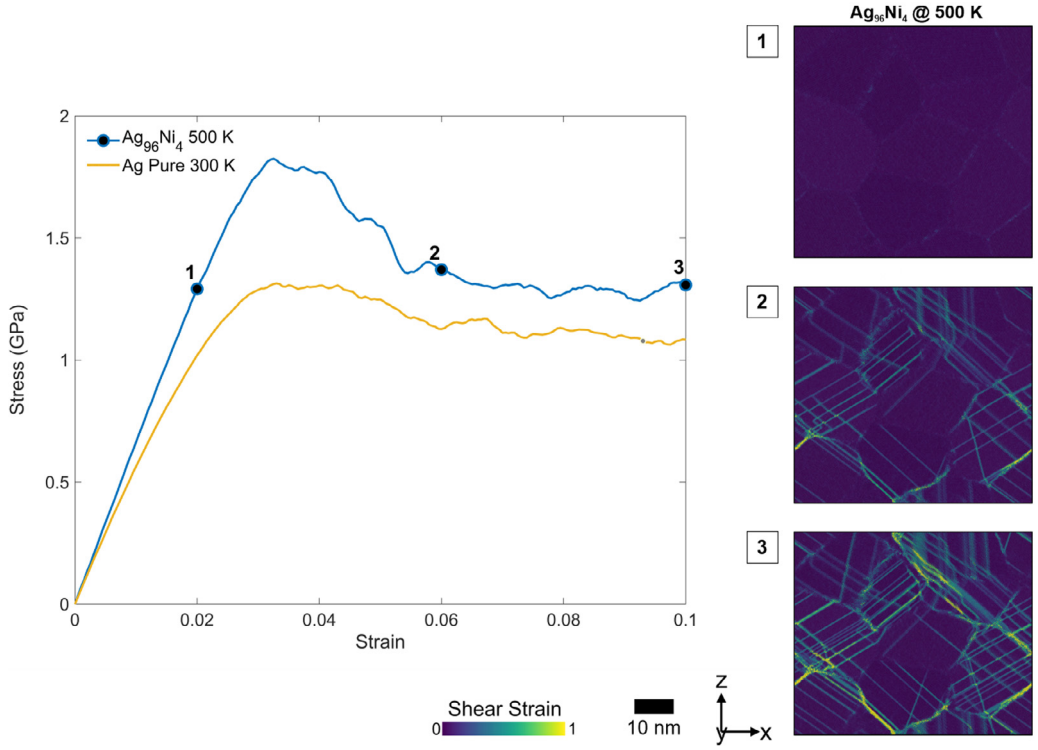

Fig. 9. Tensile stress-strain curves of pure FCC Ag and segregated FCC $Ag_{96}Ni_4$ polycrystals with atomistic snapshots of the von-Mises shear strain at different applied strain.

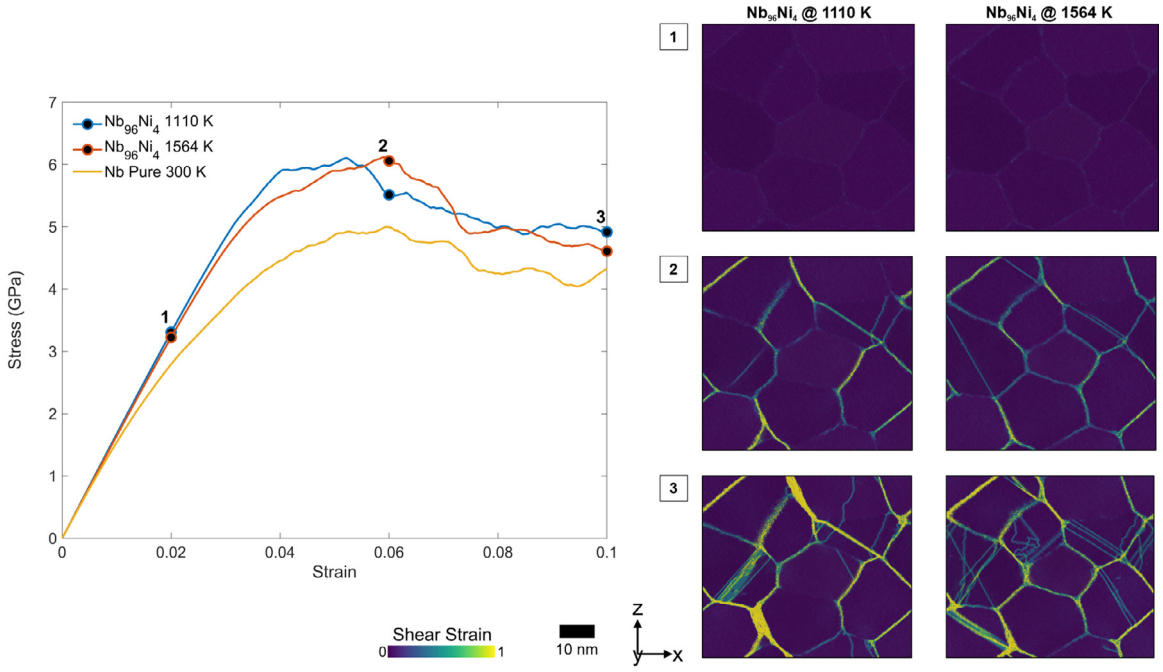

Fig. 10. Tensile stress-strain curves of pure BCC Nb and segregated BCC $Nb_{96}Ni_4$ polycrystals with atomistic snapshots of the von-Mises shear strain at different applied strain.

stress-strain curve for $Nb_{96}Ni_4$ at 1564 K shows the same shape as that in pure Nb, except for a net increase in yield strength due to GB segregation effects.

4.3. HCP Zr polycrystals

The stress-strain curves for pure Zr and $Zr_{96}Ni_4$ polycrystals segregated at 464 K and 1118 K are compared in Fig. 11. Like the $Nb_{96}Ni_4$ polycrystal at 1564 K, the $Zr_{96}Ni_4$ alloys simulated presented no clear sign of shear localization, as shown in the accompanying snapshots of deformation. All simulated curves display similar characteristics of a homogeneous plastic deformation without strain-softening region. Snapshots 3 at 464 K and 1118 K shows an increase in the branching of shearing throughout the grains and GBs from 6% to 10% applied strain, but no significant localization

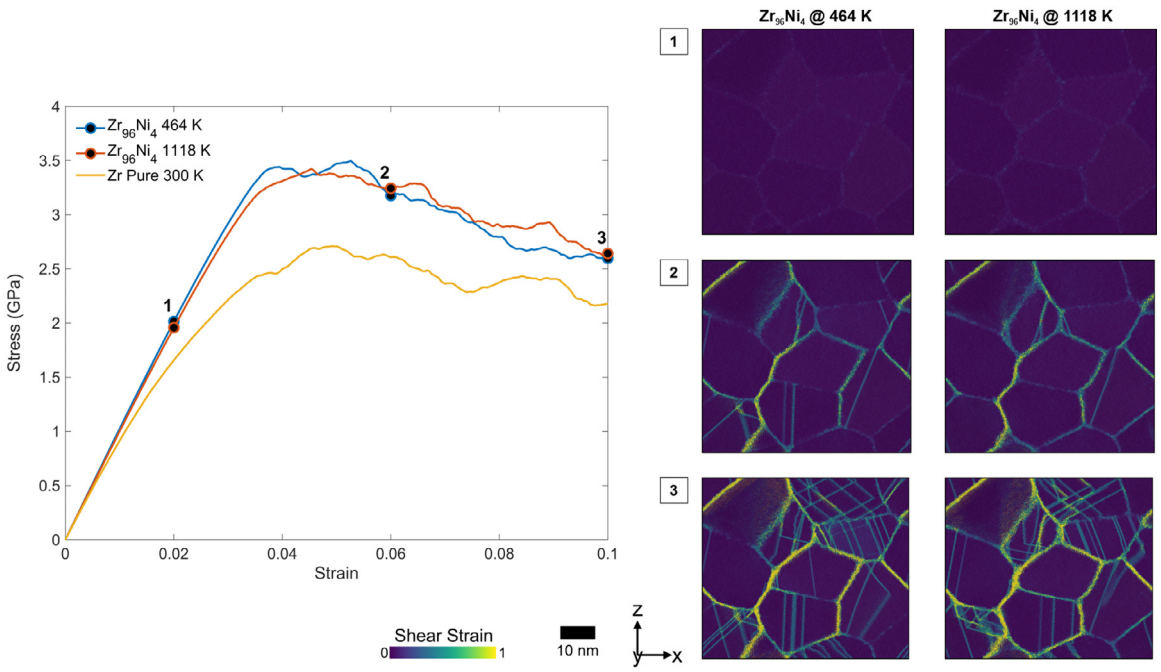

Fig. 11. Tensile stress-strain curves of pure HCP Zr and segregated HCP $Zr_{96}Ni_4$ polycrystals with atomistic snapshots of the von-Mises shear strain at different applied strain.

or shear bands comparable to those in the $Ag_{96}Ni_4$ and $Nb_{96}Ni_4$ polycrystals described above.

5. Discussion

5.1. Role of GB solute interaction on heterogeneous segregation behavior

This investigation finds that the GB segregation behavior of Ni solute atoms in the studied alloys is not exclusive to being fully heterogeneous or fully homogeneous and results in a range of segregation configurations. Ni segregation in the reference FCC $Ag_{96}Ni_4$ polycrystal agrees with predictions in the literature by presenting a strong tendency for heterogeneous segregation and Ni clustering at GBs. The BCC $Nb_{96}Ni4$ polycrystal exhibits homogeneous segregation with second-phase precipitation at GB triple junctions at the same homologous temperature (1110 K). Segregation behavior in both BCC $Nb_{96}Ni_4$ polycrystal at 1564 K and HCP $Zr_{96}Ni_4$ polycrystal at 464 K corresponds to a homogeneous segregation with a dispersion of small-scale Ni solute clusters at GBs. At the opposite of $Ag_{96}Ni_4$, only one polycrystal was found to exhibit fully homogeneous segregation, the HCP $Zr_{96}Ni_4$ polycrystal segregated at its solubility limit (1118 K), containing a perfectly amorphous GB layer with no visible Ni clustering.

Although the number of models investigated is too small for generalizing the observed segregation trends to all BCC and HCP alloy systems, we propose to account for the difference in Ni solute clustering behavior between each polycrystal, by examining the local Ni solute interactions at GBs in the three alloys. It should be noted that the available literature points to a couple of ways to measure the effects of solute-solute interactions on GB segregation by atomistic simulation. First, Pan et al. [25] have proposed a simple molecular statics (MS) method to quantify solute-solute interactions and clustering at GBs based on the concept of a solute dipole formation energy inside a GB bicrystal. The solute dipole formation energy can be understood in terms of the GB energy reduction associated with the formation of 2-atom GB solute clusters, as opposed to perfectly diluted GB solutes. This concept is therefore relevant to the difference seen in the local solute distributions across the GB network in Fig. 8. The second approach recently proposed by Matson and Schuh [17] is an MS-based spectral analysis of the GB heat of mixing at each GB atom site in a polycrystal. This method uses the average solute segregation energy of atom neighbors of a fixed solute at a specific GB site, considering only nearest bond interactions. Therefore, calculations of the local GB heat of mixing are more consistent with the RDF analysis presented above in Section 3.2.

In the following, we used both methodologies and performed MS calculations using conjugate-gradient energy minimization of solute segregation energy and solute – solute interaction energies at a chosen atom site *i* inside a GB triple for each alloy polycrystal. The calculation methods for obtaining the GB heat of mixing and GB solute dipole formation energy followed Matson and Schuh [17] and Pan et al. [25], respectively. The GB triple-junction studied was the same as that shown in Fig. 3(b), 4(c) and 6(b) for each respective alloy. For simplicity, our approach only considered substitutions at one GB atom site and not all GB sites present in the polycrystal like the spectral analysis. The results presented in Table 2 for each alloy indicate that the chosen GB atom site had high (most negative) segregation energy. A recent atomistic study [55] suggests that the GB solute interaction energy could vary strongly in the local environment of a fixed GB solute and that a more rigorous method for analyzing GB solute interaction energy is to average this value over larger environments. Therefore, the present analysis based on nearest-neighbor solute interactions remains qualitative and should only be taken as a simplified approximation.

Despite this caveat, Table 2 shows that the GB heat of mixing for Ni solutes at a GB triple junction is favorable in FCC Ag and BCC Nb (positive values) and not favorable in HCP Zr (negative value). This finding could explain why, at equivalent solute content, it is more difficult for $Zr_{96}Ni_4$ polycrystals to form large solute clusters than $Ag_{96}Ni_4$ and $Nb_{96}Ni_4$ polycrystals at the same homologous temperatures. Furthermore, Table 2 shows that the most favorable (negative) dipole formation energy is encountered in the FCC Ag-Ni alloy, and the least favorable (positive) in the BCC Nb-Ni and HCP Zr-Ni alloys. This finding suggests that long-range Ni solute interac-

Table 2
MS calculations of solute segregation energy and solute – solute interaction energies at a chosen atom site *i* inside a GB triple for each alloy polycrystal studied. ΔE_i^{seg} is the local segregation enthalpy at GB atom site *i* computed by the method of Wagih and Schuh [15]. The calculation methods for obtaining the GB heat of mixing and GB solute dipole formation energy follow Matson and Schuh [17] and Pan et al. [25], respectively. The GB triple-junction studied was the same as in Fig. 3(b), 4(c) and 6(b) for each respective alloy. See text for more details.

Alloy type	ΔE_i^{seg} (kJ/mol)	GB heat of mixing (kJ/mol)	GB solute dipole formation (eV)
FCC Ag-Ni	−2.977	9.85 ± 12.9	−0.0828 ± 0.0359
BCC Nb-Ni	−0.982	15.3 ± 14.3	0.0048 ± 0.0233
HCP Zr-Ni	−3.860	−19.47 ± 24.14	0.068± 0.022

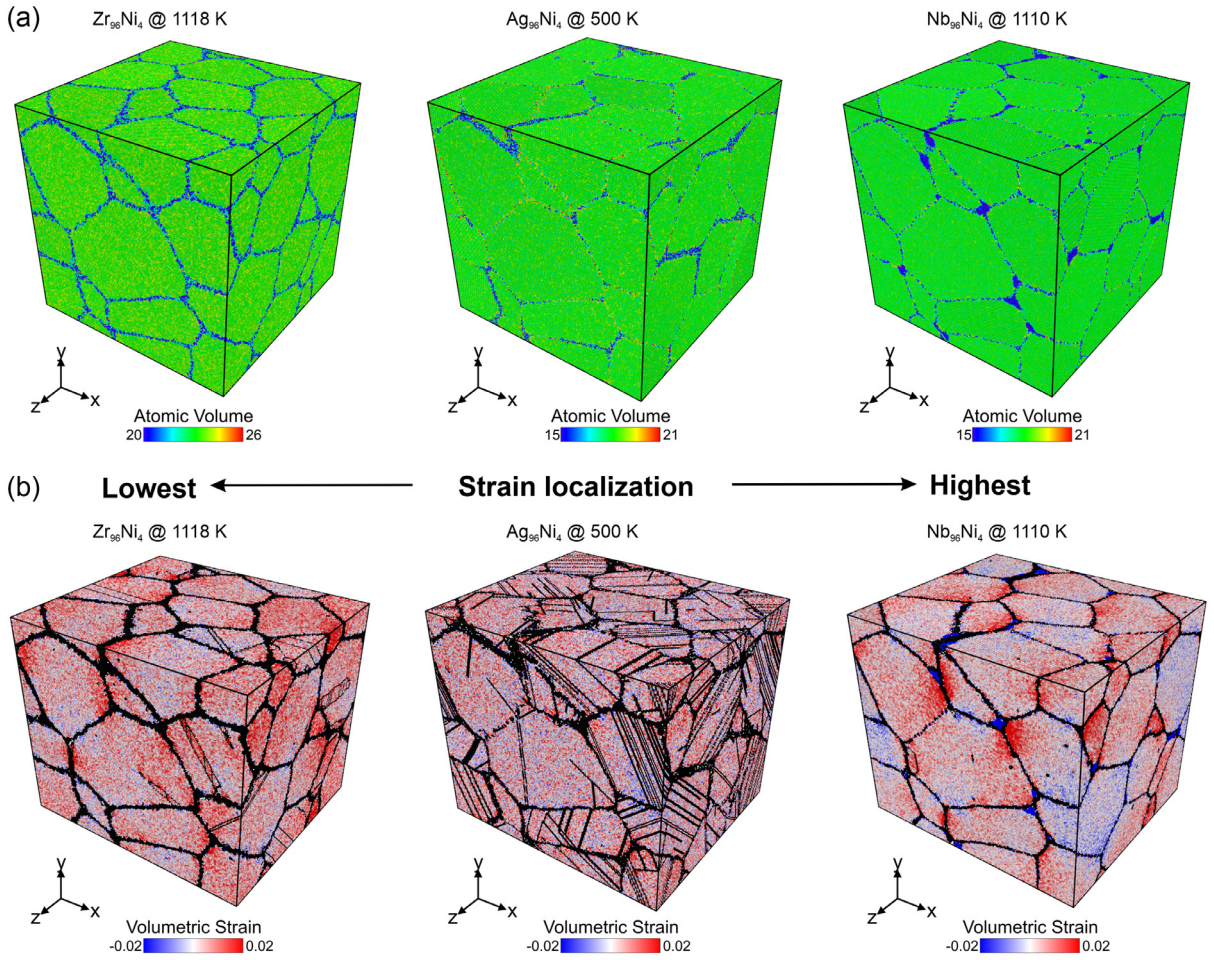

Fig. 12. Study of excess free volume expansion in $Zr_{96}Ni_4$ segregated at 1118 K, $A_{96}Ni_4$ segregated at 500 K and $Nb_{96}Ni_4$ segregated at 1110 K. (a) Atomic volume prior to deformation. (b) Volumetric strain at 9.5% applied strain. GB atoms, dislocations and stacking faults have been highlighted in dark color.

tions may facilitate large solute clustering at GB triple junctions in the $Ag_{96}Ni_4$ polycrystal, but not in the $Zr_{94}Ni_4$ and $Nb_{96}Ni_4$ polycrystals. In summary, this preliminary study suggests that considering both short-range and long-range solute interaction effects are important for rationalizing the different heterogeneous segregation phenomena observed in NC alloy polycrystals.

5.2. Physical origin of strain localization in segregated NC alloys

In this study, inspection of atomic von-Mises strain at 10% applied strain shows strain localization along GBs in the $Nb_{96}Ni_4$ polycrystal segregated at 1110 K, and to a lesser extent, in the $Ag_{96}Ni_4$ polycrystal segregated at the same homologous temperature. In addition, a salient feature in both polycrystals is that their stress-strain curve follows the typical response of amorphous and NC metals with strain localization [51]. In contrast, all pure metal polycrystals, as well as both $Zr_{96}Ni_4$ polycrystals, did not exhibit any significant shear banding during plastic deformation, but rather deformed more uniformly via standard GB sliding and dislocation plasticity mechanisms. Furthermore, shear banding was suppressed in the $Nb_{96}Ni_4$ polycrystal when the segregation temperature was raised to 1564 K to dissolve the Nb_7Ni_6 precipitates at GB triple junctions.

The above results are important in several aspects. First, the reference $Ag_{96}Ni_4$ polycrystal studied acted in the same way as the smaller polycrystal simulated by Pan and Sansoz [26] when at low Ni content, Ni clusters were not significantly large enough to impede shear localization. Second, we found in this study that the GB precipitates in the $Nb_{96}Ni_4$ polycrystal at 1110 K were present where shear localization was predominant. We hypothesized that the $Nb_{96}Ni_4$ polycrystal at 1564 K did not show shear localization because the Ni solute clusters at GB triple junctions were too small. Third, both $Zr_{96}Ni_4$ polycrystals did not show any apparent signs of shear localization despite their segregation behavior being

on the homogeneous side of the spectrum. This finding is different from past observations made in Ag-Cu alloys, where homogeneous segregation of solute atoms to GBs led to a strain path ideal for GB strain localization [26, 46, 56]. Fourth, the different crystal structure of each alloy is not considered a major factor in the type of GB segregation, as shown by the GB segregation energies calculated in Table 2, primarily because the GB network structure is amorphous. Small GB energy variations are primarily due to differences in solubility between the matrix and solute elements, atomic size mismatch, as well as the types of GB atom sites present in the different models [33].

We attribute the difference in shear localization mechanisms between the present alloy polycrystals to the expansion of excess free volume in the vicinity of large precipitates or solute clusters formed at GB triple junctions. The initial appearance of shear bands indicates plastic flow localization where shear transformation zones (STZ) [57] within the band region induce strain softening [58]. For the case for bulk metallic glasses, the formation of shear bands is influenced by local structural ordering and its microscopic variation during deformation [52]. Once formed, shear bands grow thicker due to the increase in excess free volume and void growth, until a steady-state stress plateau is reached at which point the shear band thickening stops [52, 53]. Similarly for heavily segregated NC alloys, plastic deformation is accommodated by the expansion of excess free volume and nanoscale voids within the GB network, rather than GB sliding, primarily because active solute segregation at GBs tend to block GB plasticity mechanisms [46].

To substantiate our hypothesis, we calculated in Fig. 12 the atomic volume before deformation and the volumetric strain after 9.5% applied strain in $Zr_{96}Ni_4$ segregated at 1118 K, $A_{96}Ni_4$ segregated at 500 K and $Nb_{96}Ni_4$ segregated at 1110 K, which corresponds to strain localization levels from least to most important, respectively. Fig. 12(a) shows that Ni solute segregation reduces GB energy in all cases. However, the energy reduction is uniform in the $Zr_{96}Ni_4$ polycrystal with an intergranular amorphous film, localized to GBs with highest local solute content in the heterogeneous $Ag_{96}Ni_4$ polycrystal, and strongly discontinuous in the vicinity of GB precipitates within the $Nb_{96}Ni_4$ polycrystal.

Fig. 12(b) suggests that the volumetric strain resulting from excess free volume is predicted to be the largest at GB triple junctions in the $Nb_{96}Ni_4$ polycrystal, because in this metal, less dislocations nucleate, and GB precipitation reduces GB plasticity. On the contrary, GB sliding is pervasive in the $Zr_{96}Ni_4$ polycrystal with the intergranular amorphous film, and dislocation nucleation from GB areas with low solute content provides an alternative strain accommodation mechanism in the heterogeneous $Ag_{96}Ni_4$ polycrystal. Furthermore, the deformability of $Zr_{96}Ni_4$ and $Ag_{96}Ni_4$ polycrystals is increased by the branching of shear bands to resist plastic flow throughout the system. Ni clusters in the Ag matrix have been found to reduce deformation from local shear strain and thus limited the length of shear bands. Therefore, this analysis suggests that the local solute concentration at the GB directly affected the shear strength, and Ni clusters formed by heterogeneous solute segregation acted to block the progression of shear bands.

Conclusion

Hybrid MC/MD simulations were used to study solute segregation and mechanical behavior in random FCC Ag-Ni, BCC Nb-Ni, and HCP Zr-Ni polycrystals with a focus on distinguishing homogeneous versus heterogeneous segregation behaviors. Each alloy was simulated with 4 at.% Ni solute at their maximum solubility temperature and the same homologous temperature. The RDF curve of Ni-Ni pairs in each studied binary alloy was calculated to gain insight into solute clustering at GBs. Ni-Ni dipole formation in GBs was analyzed from the intensity of the first peak of the RDF curve where a higher peak implied more significant GB solute interactions. Also, the RDF analysis provided information on the ordering of Ni atoms clusters, which helped to better understand the distribution of Ni solute atoms within GBs. Furthermore, segregation heterogeneity was studied by calculating the local density of Ni atoms in the GBs. The number of peaks present in the density distribution, indicated either homogeneous segregation or heterogeneous segregation, respectively.

It was found that segregation was not limited to being only fully heterogeneous or fully homogeneous. The types of segregation ranged from: (1) pure heterogeneous segregation ($Ag_{96}Ni_4$ at 500 K), (2) homogeneous segregation with second-phase precipitates at GB triple junctions ($Nb_{96}Ni_4$ at 1110 K), (3) homogeneous segregation with a dispersion of small-scale Ni clusters at GBs ($Nb_{96}Ni_4$ at 1564 K, $Zr_{96}Ni_4$ at 464 K), and (4) pure homogeneous segregation with amorphous intergranular films ($Zr_{96}Ni_4$ at 1118 K).

Furthermore, it was found that the different types of segregation behavior led to significant variations in stress-strain response for each alloy. Fully heterogeneous Ni segregation promoted less significant shear localization than homogeneous segregation with GB precipitation, which was associated with the most significant shear localization, compared to all cases. Homogeneous segregation with dispersion of small-scale Ni clusters and fully homogeneous segregation behaviors did not promote shear localization.

We quantified GB solute interactions in each alloy polycrystal using previously established MS methods and demonstrated that both short-range and long-range GB solute interactions contributed to the heterogeneous segregation phenomenon. Furthermore, we showed that the difference in shear localization mechanisms between the polycrystals related to the expansion of excess free volume in the vicinity of large precipitates or solute clusters formed at GB triple junctions. Therefore, this study amplifies the importance of segregation temperature and solute concentration on GB segregation behavior and associated mechanical properties in stable NC alloys. Achieving better control over the distribution and interaction of GB solutes within NC structures could be advantageous to expand the range of applications for NC materials.

Declaration of Competing Interest

The authors declare that they have no known competing financial interests or personal relationships that could have appeared to influence the work reported in this paper.

Acknowledgments

This research received support by the U.S. Department of Energy under grant No. DE-SC0020054 and used resources of the NERSC, a U.S. Department of Energy Office of Science User Facility located at Lawrence Berkeley National Laboratory, operated under Contract No. DE-AC02-05CH11231.

Supplementary materials

Supplementary material associated with this article can be found, in the online version, at doi:10.1016/j.actamat.2022.118367.

References

[1] M.A. Meyers, A. Mishra, D.J. Benson, Mechanical properties of nanocrystalline materials, Prog. Mater. Sci. 51 (4) (2006) 427–556.
[2] Y. Zou, J.M. Wheeler, H. Ma, P. Okle, R. Spolenak, Nanocrystalline high-entropy alloys: a new paradigm in high-temperature strength and stability, Nano Lett. 17 (3) (2017) 1569–1574.
[3] R. Wurschum, S. Herth, U. Brossmann, Diffusion in nanocrystalline metals and alloys - a status report, Adv. Eng. Mater. 5 (5) (2003) 365–372.

[4] J.Y. Zhao, G.X. Wang, C. Ye, Y.L. Dong, A numerical model coupling diffusion and grain growth in nanocrystalline materials, Comp Mater Sci 136 (2017) 243–252.
[5] M. Chandross, N. Argibay, Ultimate strength of metals, Phys. Rev. Lett. 124 (12) (2020) 125501.
[6] T. Chookajorn, H.A. Murdoch, C.A. Schuh, Design of stable nanocrystalline alloys, Science 337 (6097) (2012) 951–954.
[7] C.C. Koch, R.O. Scattergood, M. Saber, H. Kotan, High temperature stabilization of nanocrystalline grain size: thermodynamic versus kinetic strategies, J. Mater. Res. 28 (13) (2013) 1785–1791.
[8] F. Abdeljawad, S.M. Foiles, Stabilization of nanocrystalline alloys via grain boundary segregation: a diffuse interface model, Acta Mater. 101 (2015) 159–171.
[9] J. Weissmüller, Alloy effects in nanostructures, Nanostruct. Mater. 3 (1–6) (1993) 261–272.
[10] D. McLean, Grain Boundaries in Metals, Clarendon Press, Oxford, 1957.
[11] L. Huber, B. Grabowski, M. Militzer, J. Neugebauer, J. Rottler, Ab initio modelling of solute segregation energies to a general grain boundary, Acta Mater 132 (2017) 138–148.
[12] L. Huber, R. Hadian, B. Grabowski, J. Neugebauer, A machine learning approach to model solute grain boundary segregation, npj Computat. Mater. 4 (1) (2018) 1–8.
[13] L. Karkina, I. Karkin, A. Kuznetsov, Y. Gornostyrev, Alloying element segregation and grain boundary reconstruction, Atomist. Model., Met. 9 (12) (2019) 1319.
[14] M. Wagih, P.M. Larsen, C.A. Schuh, Learning grain boundary segregation energy spectra in polycrystals, Nat. Commun. 11 (1) (2020) 1–9.
[15] M. Wagih, C.A. Schuh, Spectrum of grain boundary segregation energies in a polycrystal, Acta Mater. 181 (2019) 228–237.
[16] M. Wagih, C.A. Schuh, Grain boundary segregation beyond the dilute limit: separating the two contributions of site spectrality and solute interactions, Acta Mater. 199 (2020) 63–72.
[17] T.P. Matson, C.A. Schuh, Atomistic assessment of solute-solute interactions during grain boundary segregation, Nanomaterials 11 (9) (2021) 2360.
[18] J.D. Rittner, D.N. Seidman, Solute-atom segregation to ⟨110⟩ symmetric tilt grain boundaries, Acta Mater. 45 (8) (1997) 3191–3202.
[19] T. Frolov, K.A. Darling, L.J. Kecskes, Y. Mishin, Stabilization and strengthening of nanocrystalline copper by alloying with tantalum, Acta Mater. 60 (5) (2012) 2158–2168.
[20] B.C. Hornbuckle, T. Rojhirunsakool, M. Rajagopalan, T. Alam, G.P. Purja Pun, R. Banerjee, K.N. Solanki, Y. Mishin, L.J. Kecskes, K.A. Darling, Effect of Ta solute concentration on the microstructural evolution in immiscible Cu-Ta alloys, JOM 67 (12) (2015) 2802–2809.
[21] C.J. O'Brien, C.M. Barr, P.M. Price, K. Hattar, S.M. Foiles, Grain boundary phase transformations in PtAu and relevance to thermal stabilization of bulk nanocrystalline metals, J. Mater. Sci. 53 (4) (2018) 2911–2927.
[22] P. Lu, F. Abdeljawad, M. Rodriguez, M. Chandross, D.P. Adams, B.L. Boyce, B.G. Clark, N. Argibay, On the thermal stability and grain boundary segregation in nanocrystalline PtAu alloys, Materialia 6 (2019) 100298.
[23] C.M. Barr, S.M. Foiles, M. Alkayyali, Y. Mahmood, P.M. Price, D.P. Adams, B.L. Boyce, F. Abdeljawad, K. Hattar, The role of grain boundary character in solute segregation and thermal stability of nanocrystalline Pt–Au, Nanoscale 13 (6) (2021) 3552–3563.
[24] N.M. Heckman, S.M. Foiles, C.J. O'Brien, M. Chandross, C.M. Barr, N. Argibay, K. Hattar, P. Lu, D.P. Adams, B.L. Boyce, New nanoscale toughening mechanisms mitigate embrittlement in binary nanocrystalline alloys, Nanoscale 10 (45) (2018) 21231–21243.
[25] Z. Pan, V. Borovikov, M.I. Mendelev, F. Sansoz, Development of a semi-empirical potential for simulation of Ni solute segregation into grain boundaries in Ag, Modelling and Simulation in, Mater. Sci. Eng. 26 (7) (2018) 075004.
[26] Z. Pan, F. Sansoz, Heterogeneous solute segregation suppresses strain localization in nanocrystalline Ag-Ni alloys, Acta Mater. 200 (2020) 91–100.
[27] K. Santhi, E. Thirumal, S. Karthick, H.-J. Kim, M. Nidhin, V. Narayanan, A. Stephen, Synthesis, structure stability and magnetic properties of nanocrystalline Ag–Ni alloy, J. Nanopart. Res. 14 (5) (2012) 1–12.
[28] X. Zhou, A. Gupta, G.J. Tucker, G.B. Thompson, Manipulation of solute partitioning mechanisms for nanocrystalline stability, Acta Mater. 208 (2021) 116662.
[29] A. Khalajhedayati, Z. Pan, T.J. Rupert, Manipulating the interfacial structure of nanomaterials to achieve a unique combination of strength and ductility, Nat. Commun. 7 (1) (2016) 10802.
[30] T. Lei, J. Shin, D.S. Gianola, T.J. Rupert, Bulk nanocrystalline Al alloys with hierarchical reinforcement structures via grain boundary segregation and complexion formation, Acta Mater. 221 (2021) 117394.
[31] G. Wu, C. Liu, L. Sun, Q. Wang, B. Sun, B. Han, J.-J. Kai, J. Luan, C.T. Liu, K. Cao, Y. Lu, L. Cheng, J. Lu, Hierarchical nanostructured aluminum alloy with ultrahigh strength and large plasticity, Nat. Commun. 10 (1) (2019) 5099.
[32] G.H. Balbus, J. Kappacher, D.J. Sprouster, F. Wang, J. Shin, Y.M. Eggeler, T.J. Rupert, J.R. Trelewicz, D. Kiener, V. Maier-Kiener, D.S. Gianola, Disordered interfaces enable high temperature thermal stability and strength in a nanocrystalline aluminum alloy, Acta Mater. 215 (2021) 116973.
[33] X. Zhou, X.-x. Yu, T. Kaub, R.L. Martens, G.B. Thompson, Grain boundary specific segregation in nanocrystalline Fe (Cr), Sci. Rep. 6 (1) (2016) 1–14.
[34] S. Plimpton, Fast parallel algorithms for short-range molecular dynamics, J Comput Phys 117 (1) (1995) 1–19.
[35] Y. Zhang, R. Ashcraft, M. Mendelev, C. Wang, K. Kelton, Experimental and molecular dynamics simulation study of structure of liquid and amorphous Ni62Nb38 alloy, J. Chem. Phys. 145 (20) (2016) 204505.
[36] M. Mendelev, M. Kramer, S. Hao, K. Ho, C. Wang, Development of interatomic potentials appropriate for simulation of liquid and glass properties of NiZr2 alloy, Philos. Mag. 92 (35) (2012) 4454–4469.
[37] B. Sadigh, P. Erhart, A. Stukowski, A. Caro, E. Martinez, L. Zepeda-Ruiz, Scalable parallel Monte Carlo algorithm for atomistic simulations of precipitation in alloys, Phys. Rev. B 85 (18) (2012) 184203.
[38] U. Kattner, B. Burton, in: ASM Handbook Volume 3: Alloy Phase Diagrams, ASM International, Geauga County, OH, USA, 1992, pp. 2–44.
[39] A. Cezairliyan, F. Righini, Thermodynamic studies of the $\alpha \rightarrow \beta$ phase transformation in zirconium using a subsecond pulse heating technique, J. Res. Natl. Bureau Standards. Sect. A, Phys. Chem. 79 (1) (1975) 81.
[40] P. Hirel, Atomsk: a tool for manipulating and converting atomic data files, Comput. Phys. Commun. 197 (2015) 212–219.
[41] Y.M. Smirnov, V. Finkel, Crystal structure of tantalum, niobium, and vanadium at 110-400K, Soviet J. Exp. Theoret. Phys. 22 (1966) 750.
[42] J.L. Zarestky, Lattice Dynamics of HCP and Bcc Zirconium, Iowa State University (1979).
[43] A. Stukowski, Visualization and analysis of atomistic simulation data with OVITO–the open visualization tool, Modell. Simul. Mater. Sci. Eng. 18 (1) (2009) 015012.
[44] M. Mahladisa, L. Ackermann, P. Ngoepe, Structural properties of gold clusters at different temperatures: : NRF /Royal Society programme, S. Afr. J. Sci. 101 (2005) 471–474.
[45] C. Kittel, P. McEuen, Kittel's Introduction to Solid State Physics, John Wiley & Sons. (2018).
[46] F. Sansoz, X. Ke, Hall-petch strengthening limit through partially active segregation in nanocrystalline Ag-Cu alloys, Acta Mater. 225 (2022) 117560.
[47] H. Turnow, H. Wendrock, S. Menzel, T. Gemming, J. Eckert, Synthesis and characterization of amorphous Ni–Zr thin films, Thin Solid Films 561 (2014) 48–52.
[48] M.Y. Sengul, C.A. Randall, A.C. Van Duin, ReaxFF molecular dynamics simulation of intermolecular structure formation in acetic acid-water mixtures at elevated temperatures and pressures, J. Chem. Phys. 148 (16) (2018) 164506.
[49] R.A. Asal, The Metal-Insulator Transition in the Amorphous Silicon-Nickel System, University of Leicester Leicester (United Kingdom, 1993.
[50] J. Ding, E. Ma, M. Asta, R.O. Ritchie, Second-nearest-neighbor correlations from connection of atomic packing motifs in metallic glasses and liquids, Sci. Rep. 5 (1) (2015) 1–9.
[51] P. Steif, F. Spaepen, J. Hutchinson, Strain localization in amorphous metals, Acta Metall. 30 (2) (1982) 447–455.
[52] Y. Jiang, Numerical modeling of cyclic deformation in bulk metallic glasses, Metals (Basel) 6 (9) (2016) 217.
[53] S. Feng, P. Yu, F. Zhao, L. Gao, N. Xu, G. Li, M. Ma, L. Qi, R. Liu, Effects of forming pores on mechanical property of Zr70Cu30 metallic glass, Mater. Res. 18 (2015) 44–48.
[54] M. De Haas, J.T.M. De Hosson, On the effects of thermomechanical processing on failure mode in precipitation-hardened aluminium alloys, J. Mater. Sci. 37 (23) (2002) 5065–5073.
[55] T. Nenninger, F. Sansoz, Local atomic environment analysis of short and long-range solute-solute interactions in a symmetric tilt grain boundary, Scr. Mater. 222 (2023) 115045.
[56] X. Ke, J. Ye, Z. Pan, J. Geng, M.F. Besser, D. Qu, A. Caro, J. Marian, R.T. Ott, Y.M. Wang, F. Sansoz, Ideal maximum strengths and defect-induced softening in nanocrystalline-nanotwinned metals, Nat. Mater. 18 (11) (2019) 1207–1214.
[57] E.S. Park, Understanding of the shear bands in amorphous metals, Appl. Microsc. 45 (2) (2015) 63–73.
[58] J.H. Perepezko, S.D. Imhoff, M.-.W. Chen, J.-.Q. Wang, S. Gonzalez, Nucleation of shear bands in amorphous alloys, Proc. Natl. Acad. Sci. 111 (11) (2014) 3938–3942.